ACS APPLIED MATERIALS & INTERFACES

Research Article

www.acsami.org

Synthesis of Anatase TiO_2 Nanosheets with Enhanced Pseudocapacitive Contribution for Fast Lithium Storage

Bo Hao, Yong Yan, Xiaobo Wang, and Ge Chen*

College of Environmental & Energy Engineering, Beijing University of Technology, Pingleyuan 100, 100124 Beijing, P.R. China

Supporting Information

ABSTRACT: Anatase TiO_2 nanosheets (ATNs) are successfully prepared by a biomimetic layer-by-layer titania mineralization approach, and the electrochemical performance of the ATNs as negative electrode for lithium-ion batteries is investigated by the galvanostatic chronopotentiometry and cyclic voltammetry. A high initial discharge capacity (311 mA h g^{-1}) and initial Coulombic efficiency (81.7%) were obtained for ATNs, and capacities of 252, 202, 186, 158, 136, and 119 mA h g^{-1} were obtained at 0.2, 1, 5, 10, 20, and 30 C, respectively. Particularly, the ATNs can still maintains a capacity of 108 mA h g^{-1} after 4000 cycles at 30 C (only a capacity loss of 10%), which indicated a superior rate capabilities and cyclability. The CVs analysis revealed that the ANTs have both diffusive lithium storage in the bulk and pseudocapacitive lithium storage at the surface (also called interfacial lithium storage), and the pseudocapacitive lithium storage dominates the total capacity when the scan rates are above 1 mV s^{-1}. The fast and stable lithium storage of ATNs might be attributed to the high pseudocapacitive lithium storage contribution in the material, and it was suggested the pseudocapacitive lithium storage could occurred at grain−grain interfaces as well as nanosheet surfaces.

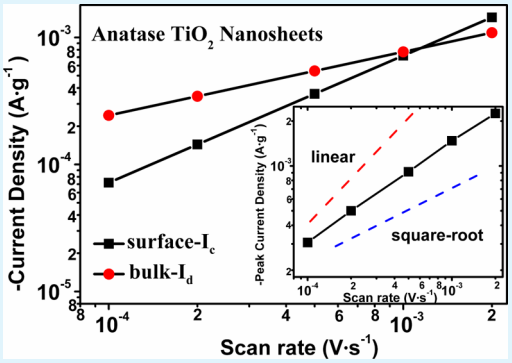

KEYWORDS: *TiO_2, nanosheet, layer-by-layer, lithium ion battery, pseudocapacity, high-rate*

INTRODUCTION

The rapidly growing demand for electric vehicles and mobile electronics urgently requires the development of lithium ion batteries (LIBs) with both high power density and high energy density, one of major challenges is to develop novel electrode materials with fast charge/discharge rate, high capacity and long cycle life.[1] Anatase TiO_2 is regarded as an ideal electrode material for fast lithium storage due to the advantages in terms of low cost, environmentally benign, structural stability, and facile approach,[2−8] moreover, its high working voltage (more than 1.7 V vs Li^+/Li) alleviate the formation of solid electrolyte interfaces layers and avoid electroplating of lithium during high rate operation.[2] However, the poor rate capability of TiO_2 electrodes, which results from their low electrical conductivity and lithium diffusion coefficient, seriously hinder its practical application in high power LIBs.[2,9] To overcome the electronic and ionic transport limitations and improve the rate performance of TiO_2-based electrodes, different strategies, such as fabricating various TiO_2 nanostructures,[10−13] coating/mixing with more conductive materials[14−20] have been developed. Particularly, the reduction of the TiO_2 particle size is of great importance to improve the rate performance because of the short path lengths for lithium diffusion and electronic transport; also, the smaller TiO_2 particle size often lead to the increase of surface areas, which result in higher electrolyte/electrode contact area, thus resulting in faster charge/discharge rates.

On the other hand, decreasing the crystallite size to nanoscale dimension leads to a significant increase of pseudocapacitve effect, which is the lithium storage occurring at the surface, also called interfacial lithium storage.[21−30] Because of its fast faradaic reactions at the surface and long-term cycling stability, the development of pseudocapacitance is of great interest for high power density applications.[31,32] This charge storage mechanism is different from lithium-ion insertion reactions that occur in LIBs and lead to high energy density; therefore, the nanosized material offer an unique opportunity to tailor power density and energy density, closing the gap between LIBs and supercapacitors. In the past decades, various nanostructured anatase TiO_2 have been fabricated and exhibited the improved electrochemical performance in LIBs;[10−13] however, the capacitve effect arising from nano-structured anatase TiO_2 have received much less attention, very few papers addressed the pseudocapacitive contribution for anatase TiO_2,[33−36] and the difficulty to separate the capacitive behavior from the diffusion-controlled insertion behavior might be a major cause. By fitting the voltammetric currents at various sweep rates to appropriate power law relationships, Lindstorm et al. investigated the capacitive contribution associated with lithium-ion insertion in mesoporous TiO_2 film;[33] Wang et al. investigated the nanoparticle dimension effect on capacitive contribution in a three-electrode cell and revealed the contribution became increasingly important when the particles

Received: April 11, 2013
Accepted: June 6, 2013
Published: June 6, 2013

   dx.doi.org/10.1021/am4013215 | ACS Appl. Mater. Interfaces 2013, 5, 6285−6291

size is reduced below 10 nm;[34] Zhu et al. investigated the pseudocapacitive effect for oriented anatase TiO_2 nanotube arrays using voltammetric analysis, and the relative contribution of pseudocapacitive storage was found to strongly depend on the scan rate.[35] Through galvanostatic chronopotentiometry, Shin et al. suggested a reversible pseudocapacitive storage mechanism for nanoporous anatase TiO_2 at high rates.[36] Nevertheless, many important issues such as morphology, polymorph, doping, surface areas, and hierarchical structure effect on pseudocapacitive lithium-ion storage have not been fully investigated, and the lithium-ion storage mechanism at the surface is not fully understood.

Herein, we report a fast and stable lithium ion storage for anatase TiO_2 nanosheets (ATNs) electrode, which is synthesized through a modified biomimetic layer-by-layer (LBL) titania mineralziation approach[37−40] The method is based on an aqueous, branched polyethyleneimine (b-PEI)-mediated layer-by-layer titania deposition to fabricate polymer/titania composite coatings on graphene oxide, so that, upon organic pyrolysis in air at 500 °C, ATNs are formed. Such a biomimetic approach to ATNs holds many favorable merits including: (1) except for organic pyrolysis, the whole procedure is carried out at room-temperature and neutral pH environment aqueous system, and no corrosive titanium precursors or chemicals are needed, indicating the synthetic pathway is "green"; (2) the resulting ATNs possess both nanosized effects and the stability of the assemblies, which will diminish some disadvantages for simple nanosized materials such as undesirable side reactions resulting from a large of surface area and poor electronic conduction network due to aggregation of nanoparticles. Galvanostatic chronopotentiometry of ATNs show a high initial Coulombic efficiency and excellent high-rate lithium storage capabilities, particularly, the ATNs maintain a capacity of 108 mA h g^{-1} after 4000 cycles at a high rate (30 C, about 5 A/g). Cyclic voltammograms revealed that the ATNs electrodes have both pseudocapacitive storage associated with surface and bulk diffusion storage, and the pseudocapacitive storage dominates the total capacity when the scan rates are above 1 mV s^{-1}; we suggest the fast and stable lithium storage performance for ATNs might be attributed from the high pseudocapacitive storage contribution at high rates, which occurred at nanocrystal interfaces as well as nanosheet surfaces.

EXPERIMENTAL SECTION

Synthesis of Anatase TiO_2 Nanosheets. A biomimetic layer by layer titania deposition approach to prepare anatase TiO_2 nanosheets is schematically illustrated in Scheme 1. At the beginning, graphene oxide solution (Graphene-supermarket) was used as the 2D template, and branched polyethyleneimine (b-PEI, Sigma-Aldrich) was used as the catalytic polymer; through an electrostatic interaction, the b-PEI was adsorbed on graphene oxide (GO) by mixing the graphene oxide solution (0.5 mg/mL, 25 mL) and buffered b-PEI solution (Tris-HCl, pH 7.0, 25 mL, 6 wt %) and stirring at room temperature for 2 h. Then the GO/b-PEI composite was centrifuged and rinsed twice with deionized water to remove the residual b-PEI. Next, the GO/b-PEI was dispersed in 20 mL of deionized water homogeneously, followed by dropwise adding 4.5 mL of titanium bis(ammonium lactato)-dihydroxide (Ti-BALDH) aqueous solution (22 g/L, pH 6.8, Alfa Aesar) to obtain the Ti−O layer upon the surface of GO/b-PEI. After being centrifuged and washed with deionized water twice, a GO/b-PEI/Ti−O composite was obtained. By repeating the above steps for 5 cycles, b-PEI/Ti−O-coated graphene oxides nanosheets were obtained. After organic pyrolysis in air at 500 °C for 3 h, anatase TiO_2 nanosheets were obtained.

Scheme 1. Illustration of the Biomimetic Layer-by-Layer Deposition Titania Assisted the Synthesis of Anatase TiO_2 Nanosheets

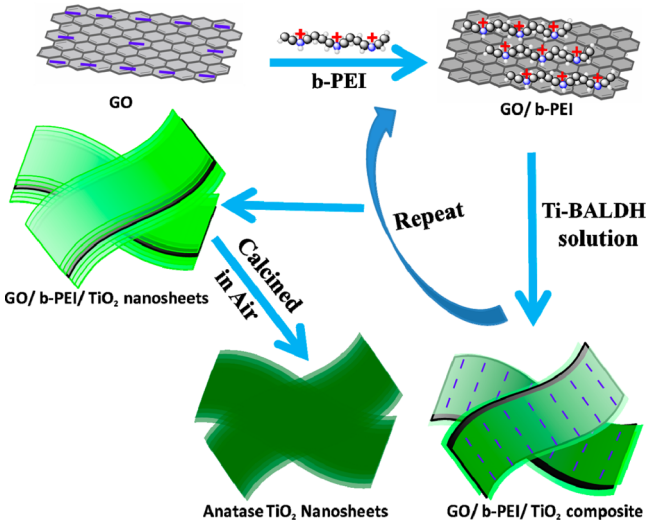

Material Characterization. The X-ray diffraction (XRD) of powder samples was examined on a Bruker D8 ADVANCE X-ray filtered Cu Kα radiation. The zeta-potentials of GO/b-PEI and GO/b-PEI/Ti−O composite were measured in water using a Zetasizer NS instrument (Malvern Instruments, Malvern). Note three zeta potential measurements were obtained from each of three different samples for each data point in Figure 1 (i.e., 9 measurements for a given stage of

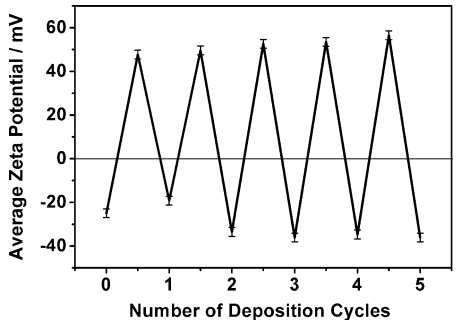

Figure 1. Zeta-potential measurement of graphene oxide after the deposition of each layer. The first measurement (layer 0) is the surface potential of graphene oxide.

exposure). Scanning electron microscope (SEM) images were obtained from a Hitachi S-4300 instrument in high vacuum mode. Transmission electron microscopy (TEM and high-resolution TEM) images were taken with a Tecnai F20 microscope equipped with EDX energy dispersive spectrometers (EDS) at an accelerating voltage of 200 kV. The nitrogen adsorption and desorption isotherms at 77 K were obtained with an Autosorb system (Quanta Chrome, USA).

Electrochemical Measurement. To prepare the working electrodes, we pasted an N-methyl pyrrolidinone (NMP) slurry, containing 75 wt % of the anatase TiO_2 nanosheets, 10 wt % polyvinylidene fluoride (Aldrich), and 15 wt % of carbon black, onto the pure Cu foil. The active material loading was 1.5−1.7 mg/cm^2. The electrodes were dried under a vacuum at 100 °C overnight. Glass fiber (GF/D Whatman) was used as a separator. The counter electrode was pure lithium foil (Aldrich) and the electrolyte was 1 M $LiPF_6$ which was a 50:50 v/v mixture of ethylene carbonate and diethyl carbonate. Cell assembly was conducted in a recirculating argon glovebox in which the moisture and oxygen content were all under 1 ppm. A Neware battery tester (Shenzhen, China) was used to conduct the Galvanostatic chronopotentiometries. Cyclic voltammetry (CV) studies were

dx.doi.org/10.1021/am4013215 | ACS Appl. Mater. Interfaces 2013, 5, 6285−6291

obtained over the potential range from 3.0 to 1.0 V at a scanning rate of 0.1, 0.2, 0.5, 1.0, and 2.0 mV s^{-1} on a potentiostat (VMP3).

RESULTS AND DISCUSSION

A modified biomimetic way through layer-by-layer titania deposition was used to convert graphene oxides into ATNs. The method is based on a previously reported, aqueous, protamine-mediated layer-by-layer titania deposition to prepare protein/titania composite coatings.[37−40] Prior work involved the deposition process on diatom frustules,[37] alumina templates,[38] sillica spheres,[39] and $CaCO_3$ spheres;[40] In the experiment, an inexpensive, artificial cationic polyelectrolyte (b-PEI) was chosen to replace protamine for b-PEI demonstrating the ability of biomineralization of TiO_2 as well as protamine. The graphene oxides were exposed in an alternating fashion to buffered aqueous solutions of b-PEI and the titania precursor (Ti-BALDH) for the layer-by-layer fabrication of a b-PEI/Ti−O coating (Scheme 1).

The polycationic b-PEI molecules bind to negatively charged graphene oxides and induce the formation of a Ti−O-bearing coating from the Ti-BALDH precursor. And the ability of b-PEI to bind to the graphene oxides or titania surfaces, enabled the layer-by-layer fabrication of a b-PEI/Ti−O-bearing composite coating on the graphene oxides. Application of this LbL deposition process was tracked via zeta potential measurements taken at every step during the first five cycles of Ti−O deposition; an oscillation for zeta potentials measurement was observed after each alternative deposition of the b-PEI and TiO_2 (Figure 1), which was consistent with the presence of positively charged b-PEI molecules or of negatively charged TiO_2, respectively. Then, the b-PEI/Ti−O-coated graphene oxides were heated at 5 °C min^{-1} to 500 °C in air and held at 500 °C for 3 h for removing water, organic pyrolysis and TiO_2 crystallization. Thermogravimetric (TG) analysis of the b-PEI/Ti−O-coated graphene oxides (see Figure S1 in the Supporting Information) showed an initial reduction (11.7%) in weight before 150 °C, which was attributed to the loss of adsorbed water; and a second larger weight reduction (36.5%) was observed from about 150 to 650 °C, which was attributed to the decomposition of graphene oxides and b-PEI. Figure 2 demonstrated the SEM image of a b-PEI/Ti−O-coated graphene oxides via exposure to 5 deposition cycles after organic pyrolysis, a large number of nanosheets with a thickness of about 30 nm were observed. Figure 3 showed the XRD pattern of the nanosheets before and after organic pyrolysis; the as prepared nanosheets (b-PEI/Ti−O-coated graphene oxides)

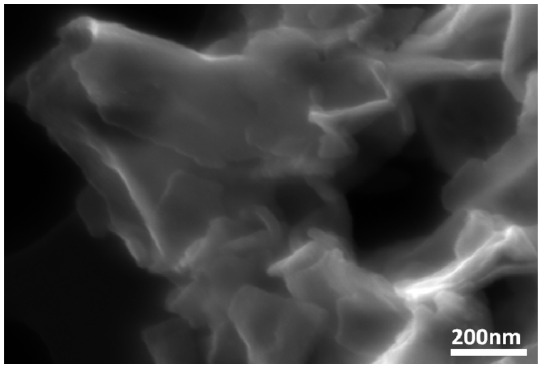

Figure 2. Scanning electron microscopy image of anatase TiO_2 nanosheets, bar: 200 nm.

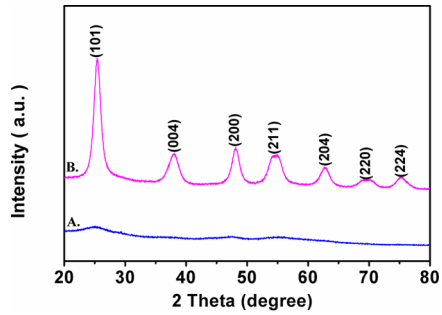

Figure 3. X-ray diffraction (XRD) pattern of the nanosheets (A) before and (B) after organic pyrolysis.

displayed amorphous structure, whereas the diffraction peaks matched well with the standard pattern of anatase (JCPDS card no. 21−1272) for nanosheets after organic pyrolysis, and the calculated average crystallite sizes (using the Scherrer formula) in the (101) direction is 5.4 ± 0.2 nm.

Figure 4a revealed the TEM images of samples after organic pyrolysis, the sheet-like structures were also observed; the

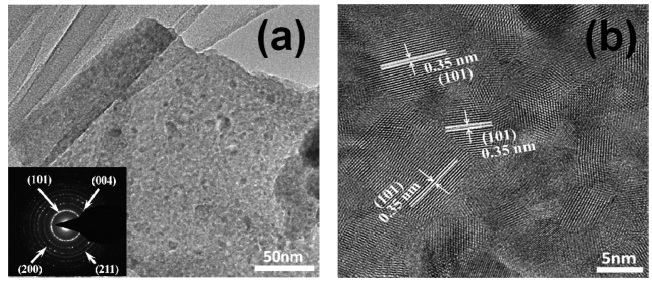

Figure 4. (a) Transmission electron microscopy image of anatase TiO_2 nanosheets; bar, 50 nm; inset, selected-area electron diffraction of anatase TiO_2 nanosheets. (b) High-resolution transmission electron microscopy image of anatase TiO_2 nanosheets; bar, 5 nm; the lattice spacings of 0.35 nm was attributed to the (101) reflections from the anatase TiO_2.

energy-dispersive X-ray spectroscopy analysis indicated the existence of Cu (from the Cu grid), Ti and O species, and the atomic ratio of O/Ti was about 2:1 (see Figure S2 in the Supporting Information), selected-area electron diffraction (SAED) showed a typical multiple rings pattern (inset in Figure 4a), and lattice planes of the anatase (101), (004), (200), and (211) were clearly indexed in SAED patterns, suggesting the obtained nanosheet is an anatase TiO_2 polycrystalline. High resolution TEM image (Figure 4b) further showed the obtained TiO_2 nanosheet was composed of numerous nanocystals (5−10 nm) connected compactly.

The nitrogen adsorption/desorption isotherms measurement conducted at 77 K (see Figure S3 in the Supporting Information) suggested the obtained ANTs was nonporous, and the BET surface area was 32 m^2 g^{-1}.

As a comparsion, the characterizations of XRD, TEM, HRTEM and BET for the commercial anatase TiO_2 nanoparticles (*Comm.*-TiO_2, Alfa aesar) were shown in Figures S4−S6 in the Supporting Information. The calculated average grain size of anatase phase (101) plane (using Scherrer formula) is about 12 nm (see Figure S4 in the Supporting Information). Figure S5 in the Supporting Informationshows a TEM image of the *Comm.*-TiO_2. It can be shown that the *Comm.*-TiO_2 comprised large particles aggregated by numerous nano-

dx.doi.org/10.1021/am4013215 | ACS Appl. Mater. Interfaces 2013, 5, 6285−6291

crystallites. High-resolution TEM image was shown in Figure S5b in the Supporting Information, a lattice spacing of 0.35 nm was observed, corresponding to the (101) plane of the anatase TiO_2. Besides, a high surface area of 178 $m^2\ g^{-1}$ was obtained in *Comm.*-TiO_2 (see Figure S6 in the Supporting Information).

The lithium-storage performance of ATNs was evaluated, for comparsion, the performance of commercial 12 nm sized anatase TiO_2 nanoparticles (*Comm.*-TiO_2, Alfa aesar) with high surface area (178 $m^2\ g^{-1}$) was also tested under the same conditions. In general, the lithium insertion/extraction reaction in anatase TiO_2 nanosheet according to the following equations

$$TiO_2 + xLi^+ + xe^- = Li_xTiO_2 \quad (1)$$

The x is the amount of inserted Li^+ in TiO_2 and it depends upon the properties of the materials used; for anatase, the maximum x is 0.5 for fully reversible reaction, accompanied with the phase transformation from the tetragonal TiO_2 to orthorhombic $Li_{0.5}TiO_2$, corresponding to a capacity of 168 mA h g^{-1}; when $x > 0.5$, the reaction known becoming very slow.[41]

Figure 5a shows the initial galvanostatic discharge/charge curves for ATNs and *Comm.*-TiO_2 conducted at a rate of 0.2 C in the potential window of 1.0−3.0 V (1 C = 168 mA g^{-1}), a high initial discharge capacity of 311.2 mA h g^{-1} and a charge capacity of 254.6 mA h g^{-1} were obtained for ATNs, corresponding to only 18.3% initial capacity loss. While the *Comm.*-TiO_2 demonstrates an initial discharge capacity of 274.6 mA h g^{-1} and a charge capacity of 205.3 mA h g^{-1}, corresponding to 24.8% initial capacity loss. Irreversible capacity loss during the first cycle is common for nanosized TiO_2 and has been attributed to surface reactions with the electrolyte on reduction,[42−47] the improvement in initial Coulombic efficiency for ATNs is important for LIBs practical applications, and might be attributed to the relative low surface areas (32 $m^2\ g^{-1}$). According to literature,[41,48−50] the discharge curve of anatase TiO_2 nanosheets can be divided into three voltage regions; in the first region, the potential decreased rapidly to about 1.7 V (vs Li^+/Li), which is attributed to a homogeneous lithium insertion to the bulk (forming solid solution domain, Li_xTiO_2 with x up to 0.15); in the second region, the potential of the anatase TiO_2 nanosheets electrode reaches a plateau at 1.7 V, where Li-rich phase (Li_xTiO_2, $0.15 < x < 0.5$) are expected to coexist anatase TiO_2 phase, this plateau signifies the biphasic region, which is typical for Li insertion into anatase TiO_2 electrode. Compared with the observed flat plateau for *Comm.*-TiO_2, the ATNs demonstrated a small decrease of potential with the increase of capacity. In the third region, the potential decreased linearly from 1.75 to 1.0 V with the increasing capacity, signifying the further Li storage occurred at nanoparticle surface/interfaces; it was suggested such Li storage is irreversible at low rates, and the reversible storage of lithium can possibly occur during this voltage region at high rates.[35] Note the ATNs possess a longer the third region than *Comm.*-TiO_2, indicating more lithium storage in this region.

Figure 5b displays the rate performance of ATNs and *Comm.*-TiO_2 at charge/discharge rate between 0.2 and 30 C; the ATNs show excellent rate performance with 186 mA h g^{-1} at 5 *C*, 158 mA h g^{-1} at 10 *C*, 136 mA h g^{-1} at 20 *C* and 119 mA h g^{-1} at 30 *C*, whereas *Comm.*-TiO_2 only maintain 126 mA h g^{-1} at 5 *C*, 108 mA h g^{-1} at 10 *C*, 87 mA h g^{-1} at 20 *C*, and 73 mA h g^{-1} at 30 *C*. To test the cycle performance for ATNs at high rates, we discharged/charged the cell at 30 *C* for 4000 cycles after aging at 5 *C* for 50 cycles. Figure 5c demonstrates

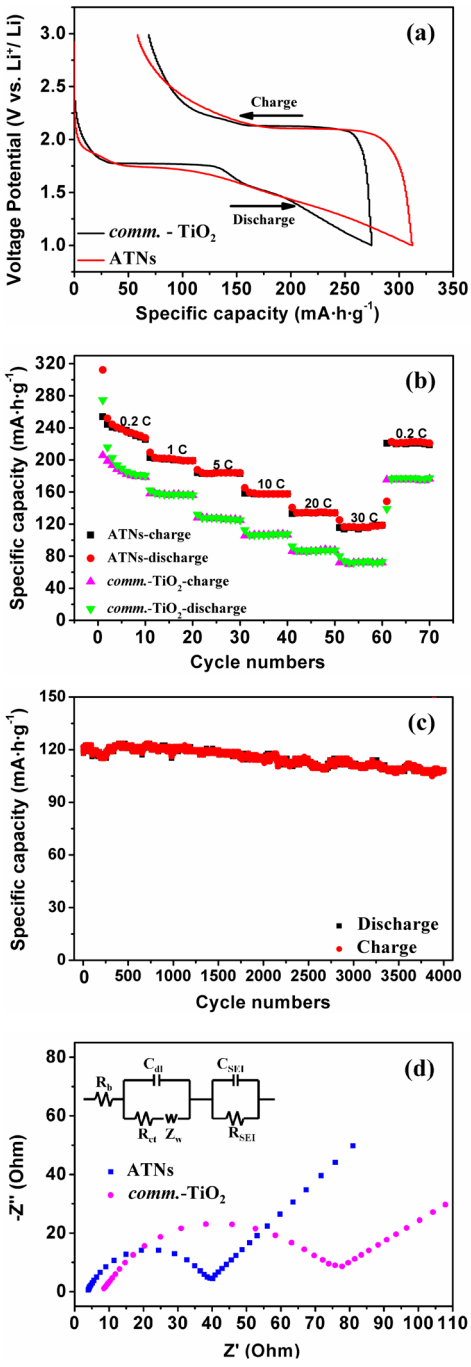

Figure 5. (a) Initial galvanostatic discharge/charge profiles for ATNs and *comm.*-TiO_2 electrodes; (b) the rate performance of ATNs and *comm.*-TiO_2 electrodes at different current rates; (c) cycling performance of ATNs electrode at high current rate of 30 C; (d) the impedance spectrum for ATNs and *comm.*- TiO_2 electrodes.

the capacity of ATNs starts at 119 mA h g^{-1} and still keeps at 108 mA h g^{-1} after 4000 cycles, which indicated a superior long-term, high-rate lithium storage capabilities. Figure 5d. represented that the impedance spectra results, the anatase TiO_2 nanosheets electrode showed a much lower Ohmic resistance (R_Ω) (3.9 Ω vs 8.5 Ω) and charge-transfer resistance (R_{ct}) (36.2 Ω vs 68.6 Ω) than commercial TiO_2 nanoparticles, which would faciliate the lithium ion transport for anatase TiO_2 nanosheet during lithium insertion/extraction process, and lead to the improved electrode performance.

dx.doi.org/10.1021/am4013215 | *ACS Appl. Mater. Interfaces* 2013, 5, 6285−6291

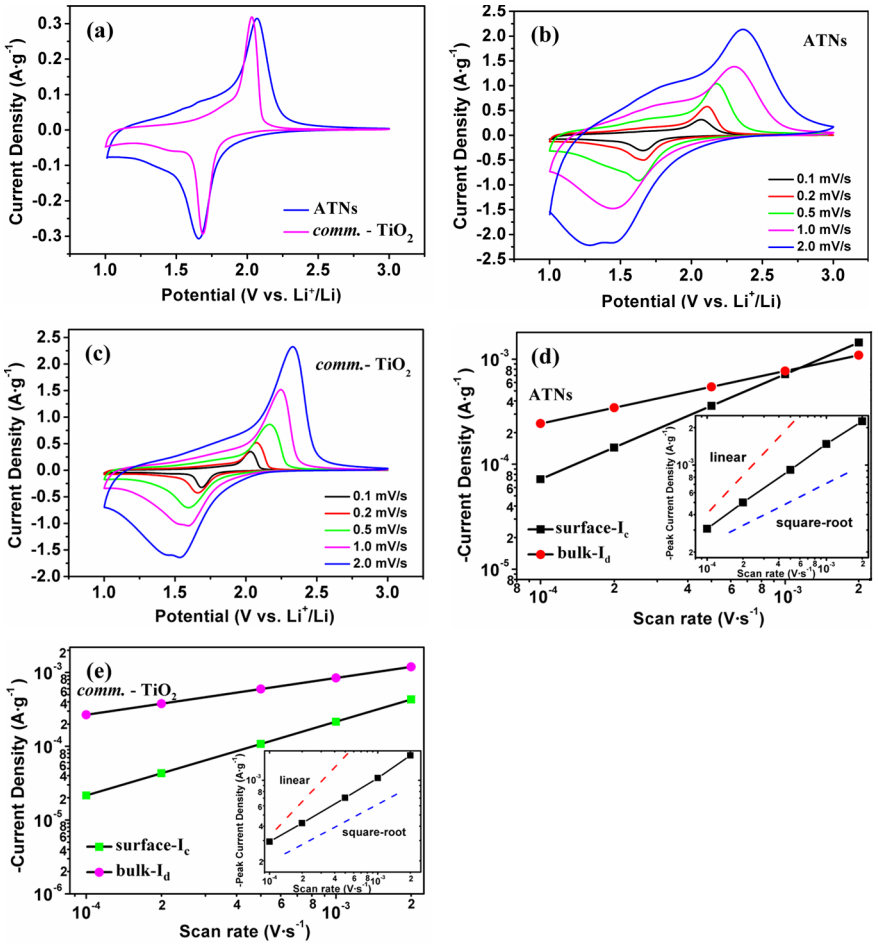

Figure 6. (a) Cyclic voltammograms of ATNs and *comm.*-TiO_2 electrodes at a scan rate of 0.1 mV s^{-1}; (b) cyclic voltammograms of ATNs electrodes at various scan rates. (c) cyclic voltammograms of *comm.*-TiO_2 electrodes at various scan rates. (d) calculated surface pseudocapacitive and bulk insertion discharge currents; insert: the peak discharge current of the ATNs measured at various scan rates. (e) Calculated surface pseudocapacitive and bulk insertion discharge currents; insert: the peak discharge current of the *comm.*-TiO_2 measured at various scan rates.

Figure 6a shows typical cyclic voltammetry (CV) curves of the ATNs and *Comm.*-TiO_2 electrode measured at a scan rate of 0.1 mVs^{-1}. The CV curve of ATNs show a couple of cathodic/anodic peaks at 1.65 and 2.06 V respectively, corresponding to Li^+ insertion/extraction potentials for the anatase TiO_2; note the potentials of the cathodic peak is a little lower than that of *Comm.*-TiO_2 (1.68 V), which agreed well with the galvanostatic chronopotentiometry. Besides the major peak, a shoulder peak was observed at 1.3−1.4 V for both ATNs and *Comm.*-TiO_2, which might be attributed to the further lithium storage occurring at nanoparticle surfaces/interfaces, note the shoulder peak of ATNs is obviously bigger than that of *Comm.*-TiO_2. The intensities of cathodic and anodic currents increased with the increase in scan rates in the whole potential window for both samples (Figure 6b, c); particularly, the intensities of shoulder peak current of ATNs increased much more than that of *Comm.*-TiO_2. The Figure 6d inset displays the relationship between the peak discharge current (I_p) and the scan rate (v) for ATNs; a power-law dependence yields $I_p \propto v^{0.9}$, and the exponent value of 0.9 could be attributed to a mixed process which involved the insertion of lithium in the bulk of TiO_2 ($I_p \propto v^{0.5}$) and the pseudocapacitive storage of lithium at the TiO_2 surface ($I_p \propto v$). It was reported that a mixed lithium storage process[33] can be expressed in the followed equation

$$I_p = C_1 v + C_2 v^{1/2} \quad (2)$$

where I_p represents the peak discharge current, v represents the scan rate, and $C_1 v$ and $C_2 v^{1/2}$ correspond to the current contributions from the pesudocapacitive effect (I_c) and lithium insertion process (I_d); by determining C_1 and C_2, we can separate the contributions of the two processes.

To facilitate the analysis, rewrite eq2 into the following format,

$$I_p/v^{1/2} = C_1 v^{1/2} + C_2 \quad (3)$$

In eq 3, C_1 and C_2 correspond to the slope and the y-axis intercept point of the peak current straight line, respectively. The fit of the data to eq 3 (see Figure S7 in the Supporting Information) yields C_1 = 0.719 ± 0.033 and C_2 = 0.024 ± 0.002. Thus, the I_c and I_d at different rates can be determined, which can be used to evaluate the relative contribution of surface and bulk storages of lithium for the ANTs and *Comm.*-TiO_2. Figure 6d shows the calculated surface pesudocapacitive current (I_c) and lithium diffusion-controlled current (I_d) with the scan rate for ANTs. At a low scan rate (0.1 mV s^{-1}), the I_c is much smaller than I_d, indicating that the lithium insertion bulk process is the predominant contribution to the whole storage. Both I_d and I_c increased with the increase of the scan rates, however, the ratio of I_c/I_d also increased, and the I_c is

dx.doi.org/10.1021/am4013215 | ACS Appl. Mater. Interfaces 2013, 5, 6285−6291

bigger than I_d when the scan rate >1 mV s^{-1}, suggesting the pesudocapacitive storage dominated the total storage at high scan rates. Figure S8 in the Supporting Information demonstrates the dependence of the $I_p/v^{1/2}$ on the square root of scan rate ($v^{1/2}$) for *Comm.*-TiO_2, and the fit of the data to eq 3 yields C_1 = 0.216 ± 0.012 and C_2 = 0.027 ± 0.003; Figure 6e shows the calculated I_d and I_c for *Comm.*-TiO_2 with the scan rate, which showed a similar trend with ANTs; however, the I_d is still bigger than I_c at high scan rates, although the ratio of I_c/I_d increased with the increase in scan rate. The result suggested the ATNs possessed a higher peseduocapacitve storage than *Comm.*-TiO_2 at high scan rates, which might lead to its improved rate performance. Obviously, the pseudocapacitive storage is dependent on the surface areas of the electrode, and thus, the obtained result is interesting for the obtained ANTs possessing a much lower surface area (32 m^2 g^{-1}) than that of *Comm.*-TiO_2 (178 m^2 g^{-1}). The explanation might be that the unique structure of ATNs possess numerous nanograin boundarys, which might provide enough active sites for pesudocapacitive lithium storage;[21,26] also, considering the accumulation of electrons at the grain−grain interface, the nanograins in ATNs might form a electronic transport path;[51] thus, the pseudocapacitive lithium storage could occurred at nanocrystal interfaces as well as nanosheet surfaces. As a consequence, high pseduocapacitive lithium storage was obtained for ATNs at high rates despite its relative low specific surface areas.

CONCLUSION

Through a biomimetic layer-by-layer titania deposition, the polymer/titania coating on graphene oxide was obtained, so that, upon organic pyrolysis in air at 500 °C, anatase TiO_2 nanosheets (ATNs) were obtained. We have investigated the electrochemical properties of ATNs as negative electrode material for LIBs by galvanostatic chronopotentiometry and CVs; the ATNs delivered a high initial Coulombic efficiency, an improved rate capability and a high stable cyclability; particularly, it maintains a capacity of 108 mA h g^{-1} after 4000 cycles at 30 C. The CVs analysis revealed that the ANTs have both diffusive lithium storage in bulk material and pseudocapacitive lithium storage at the surface, and the relative contributions of surface pseudocapacitive dominates the total storage capacity when the scan rates are above 1 mV s^{-1}. The fast and stable lithium storage of ATNs might be attributed to the high pseudocapacitive lithium storage contribution in the material, and it was suggested the pseudocapacitive lithium storage could occur at grain−grain interfaces as well as nanosheet surfaces. The obtained results help in understanding the pseudocapacitive lithium storage for anatase TiO_2 and might provide a novel approach to improve the capacity and the rate capability of the electrode materials.

ASSOCIATED CONTENT

Supporting Information

TG, EDX, XRD, TEM, HRTEM, and BET measurement results, This information is available free of charge via the Internet at http://pubs.acs.org/

AUTHOR INFORMATION

Corresponding Author

*E-mail: chenge@bjut.edu.cn.

Author Contributions

The manuscript was written through contributions of all authors. All authors have given approval to the final version of the manuscript.

Notes

The authors declare no competing financial interest.

ACKNOWLEDGMENTS

This work was supported by the National Natural Science Foundation of China (NSFC 21001012) and Beijing Nova Program (2009B06) and the Scientific Research Common Program of Beijing Municipal Commission of Education (KM201210005005)

REFERENCES

(1) Tarascon, J. M.; Armand, M. *Nature* **2001**, *414* (6861), 359−367.
(2) Yang, Z. G.; Choi, D.; Kerisit, S.; Rosso, K. M.; Wang, D. H.; Zhang, J.; Graff, G.; Liu, J. *J. Power Sources* **2009**, *192* (2), 588−598.
(3) Berger, T.; Monllor-Satoca, D.; Jankulovska, M.; Lana-Villarreal, T.; Gomez, R. *Chemphyschem.* **2012**, *13* (12), 2824−2875.
(4) Froeschl, T.; Hoermann, U.; Kubiak, P.; Kucerova, G.; Pfanzelt, M.; Weiss, C. K.; Behm, R. J.; Huesing, N.; Kaiser, U.; Landfester, K.; Wohlfahrt-Mehrens, M. *Chem. Soc. Rev.* **2012**, *41* (15), 5313−5360.
(5) Kavan, L. *Chem. Rec.* **2012**, *12* (1), 131−142.
(6) Kavan, L.; Murakami, T. N.; Comte, P.; Graetzel, M. *Electrochem. Solid-State Lett.* **2007**, *10* (4), A85−A87.
(7) Su, X.; Wu, Q. L.; Zhan, X.; Wu, J.; Wei, S. Y.; Guo, Z. H. *J. Mater. Sci.* **2012**, *47* (6), 2519−2534.
(8) Zhu, G. N.; Wang, Y. G.; Xia, Y. Y. *Energy Environ. Sci.* **2012**, *5* (5), 6652−6667.
(9) Yoon, S.; Ka, B. H.; Lee, C.; Park, M.; Oh, S. M. *Electrochem. Solid-State Lett.* **2009**, *12* (2), A28−A32.
(10) Su, X.; Wu, Q. L.; Zhan, X.; Wu, J.; Wei, S. Y.; Guo, Z. H. *J. Mater. Sci.* **2012**, *47* (6), 2519−2534.
(11) Deng, D.; Kim, M. G.; Lee, J. Y.; Cho, J. *Energy Environ. Sci.* **2009**, *2* (8), 818−837.
(12) Chen, J. S.; Lou, X. W. *Mater. Today* **2012**, *15* (6), 246−254.
(13) Chen, J. S.; Archer, L. A.; Lou, X. W. *J. Mater. Chem.* **2011**, *21* (27), 9912−9924.
(14) Moriguchi, I.; Hidaka, R.; Yamada, H.; Kudo, T.; Murakami, H.; Nakashima, N. *Adv. Mater.* **2006**, *18* (1), 69−73.
(15) Wang, D. H.; Choi, D. W.; Li, J.; Yang, Z. G.; Nie, Z. M.; Kou, R.; Hu, D. H.; Wang, C. M.; Saraf, L. V.; Zhang, J. G.; Aksay, I. A.; Liu, J. *Acs Nano* **2009**, *3* (4), 907−914.
(16) Yang, S. B.; Feng, X. L.; Mullen, K. *Adv. Mater.* **2011**, *23* (31), 3575−3579.
(17) Li, N.; Liu, G.; Zhen, C.; Li, F.; Zhang, L. L.; Cheng, H. M. *Adv. Funct. Mater.* **2011**, *21* (9), 1717−1722.
(18) Nam, S. H.; Shim, H. S.; Kim, Y. S.; Dar, M. A.; Kim, J. G.; Kim, W. B. *ACS Appl. Mater. Interfaces* **2010**, *2* (7), 2046−2052.
(19) He, B. L.; Dong, B.; Li, H. L. *Electrochem. Commun.* **2007**, *9* (3), 425−430.
(20) Guo, Y. G.; Hu, Y. S.; Sigle, W.; Maier, J. *Adv. Mater.* **2007**, *19* (16), 2087−2091.
(21) Jamnik, J.; Maier, J. *Phys. Chem. Chem. Phys.* **2003**, *5* (23), 5215−5220.
(22) Balaya, P.; Bhattacharyya, A. J.; Jamnik, J.; Zhukovskii, Y. F.; Kotomin, E. A.; Maier, J. *J. Power Sources* **2006**, *159* (1), 171−178.
(23) Conway, B. E.; Birss, V.; Wojtowicz, J. *J.Power Sources* **1997**, *66* (1−2), 1−14.
(24) Balaya, P. *Energy Environ. Sci.* **2008**, *1* (6), 645−654.
(25) Guo, X. W.; Fang, X. P.; Mao, Y.; Wang, Z. X.; Wu, F.; Chen, L. Q. *J. Phys. Chem. C* **2011**, *115* (9), 3803−3808.
(26) Yu, X. Q.; Sun, J. P.; Tang, K.; Li, H.; Huang, X. J.; Dupont, L.; Maier, J. *Phys. Chem. Chem. Phys.* **2009**, *11* (41), 9497−9503.
(27) Lai, C.; Dou, Y. Y.; Li, X.; Gao, X. P. *J. Power Sources* **2010**, *195* (11), 3676−3679.

(28) Li, X.; Lai, C.; Xiao, C. W.; Gao, X. P. *Electrochim. Acta* **2011**, *56* (25), 9152−9158.
(29) Wu, X. L.; Jiang, L. Y.; Cao, F. F.; Guo, Y. G.; Wan, L. J. *Adv. Mater.* **2009**, *21* (25−26), 2710−2714.
(30) Jiang, C. H.; Wei, M. D.; Qi, Z. M.; Kudo, T.; Honma, I.; Zhou, H. S. *J. Power Sources* **2007**, *166* (1), 239−243.
(31) Winter, M.; Brodd, R. J. *Chem. Rev.* **2004**, *104* (10), 4245−4269.
(32) Arico, A. S.; Bruce, P.; Scrosati, B.; Tarascon, J. M.; Van Schalkwijk, W. *Nat. Mater.* **2005**, *4* (5), 366−377.
(33) Lindstrom, H.; Sodergren, S.; Solbrand, A.; Rensmo, H.; Hjelm, J.; Hagfeldt, A.; Lindquist, S. E. *J. Phys. Chem. B* **1997**, *101* (39), 7717−7722.
(34) Wang, J.; Polleux, J.; Lim, J.; Dunn, B. *J. Phys. Chem. C* **2007**, *111* (40), 14925−14931.
(35) Zhu, K.; Wang, Q.; Kim, J. H.; Pesaran, A. A.; Frank, A. J. *J. Phys. Chem. C* **2012**, *116* (22), 11895−11899.
(36) Shin, J. Y.; Samuelis, D.; Maier, J. *Adv. Funct. Mater.* **2011**, *21* (18), 3464−3472.
(37) Fang, Y. N.; Wu, Q. Z.; Dickerson, M. B.; Cai, Y.; Shian, S.; Berrigan, J. D.; Poulsen, N.; Kroger, N.; Sandhage, K. H. *Chem. Mater.* **2009**, *21* (24), 5704−5710.
(38) Berrigan, J. D.; Kang, T. S.; Cai, Y.; Deneault, J. R.; Durstock, M. F.; Sandhage, K. H. *Adv. Funct. Mater.* **2011**, *21* (9), 1693−1700.
(39) Haase, N. R.; Shian, S.; Sandhage, K. H.; Kroger, N. *Adv. Funct. Mater.* **2011**, *21* (22), 4243−4251.
(40) Jiang, Y. J.; Yang, D.; Zhang, L.; Sun, Q. Y.; Sun, X. H.; Li, J.; Jiang, Z. Y. *Adv. Funct. Mater.* **2009**, *19* (1), 150−156.
(41) Wagemaker, M.; Borghols, W. J. H.; Mulder, F. M. *J. Am. Chem. Soc.* **2007**, *129* (14), 4323−4327.
(42) Poizot, P.; Laruelle, S.; Grugeon, S.; Dupont, L.; Tarascon, J. M. *Nature* **2000**, *407* (6803), 496−499.
(43) Wang, Q.; Wen, Z.; Li, J. *Inorg. Chem.* **2006**, *45* (17), 6944−6949.
(44) Hu, Y. S.; Kienle, L.; Guo, Y. G.; Maier, J. *Adv. Mater.* **2006**, *18* (11), 1421−1426.
(45) Jiang, C.; Honma, I.; Kudo, T.; Zhou, H. *Electrochem. Solid-State Lett.* **2007**, *10* (5), A127−A129.
(46) Borghols, W. J. H.; Luetzenkirchen-Hecht, D.; Haake, U.; Chan, W.; Lafont, U.; Kelder, E. M.; van Eck, E. R. H.; Kentgens, A. P. M.; Mulder, F. M.; Wagemaker, M. *J. Electrochem. Soc.* **2010**, *157* (5), A582−A588.
(47) Brutti, S.; Gentili, V.; Reale, P.; Carbone, L.; Panero, S. *J. Power Sources* **2011**, *196* (22), 9792−9799.
(48) Guo, Y. G.; Hu, Y. S.; Maier, J. *Chem. Commun.* **2006**, *26*, 2783−2785.
(49) Kavan, L.; Gratzel, M.; Rathousky, J.; Zukal, A. *J. Electrochem. Soc.* **1996**, *143* (2), 394−400.
(50) Sudant, G.; Baudrin, E.; Larcher, D.; Tarascon, J. M. *J. Mater. Chem.* **2005**, *15* (12), 1263−1269.
(51) Saravanan, K.; Ananthanarayanan, K.; Balaya, P. *Energy Environ. Sci.* **2010**, *3* (7), 939−948.